A multilayer sigma-coordinate thermodynamic sea ice model: Validation against Surface Heat Budget of the Arctic Ocean (SHEBA)/Sea Ice Model Intercomparison Project Part 2 (SIMIP2) data

H. Huwald[1]
Institute for Atmospheric and Climate Science, Swiss Federal Institute of Technology, Zurich, Switzerland

L.-B. Tremblay
Lamont-Doherty Earth Observatory, Columbia University, Palisades, New York, USA

H. Blatter
Institute for Atmospheric and Climate Science, Swiss Federal Institute of Technology, Zurich, Switzerland

Received 16 February 2004; revised 7 March 2005; accepted 16 March 2005; published 14 May 2005.

[1] A new multilayer sigma-coordinate thermodynamic sea ice model is presented. The model employs a coordinate transformation which maps the thickness of the snow and ice slabs onto unity intervals and thus enables automatic relayering when the snow or ice thickness changes. This is done through an advection term which naturally appears in the transformed energy equation. Unlike previous approaches, the model conserves the total energy per layer (Jm^{-2} as opposed to Jm^{-3}), which takes into account the changes in internal energy associated with thickness changes. This model was then tested against observational data from the Surface Heat Budget of the Arctic Ocean (SHEBA) experiment in the context of the Sea Ice Model Intercomparison Project, Part 2, Thermodynamics (SIMIP2). In general, the model reproduces the observed internal snow-ice temperature and the ice thickness evolution very well. Results show that the ice thickness evolution is very sensitive to the ocean heat flux (F_{ocn}) and the thickness of the snow cover in winter. Given that the spatial variability in snow depth at small scale is large, the specification of the snow depth temporal evolution is crucial for an intercomparison project. Since F_{ocn} in SIMIP2 is calculated as a residual of the observed basal growth rates and heat conduction, the salinity of newly formed ice used in the simulations must be consistent with that used to derive F_{ocn}. Simulated and observed snow surface and snow-ice interface temperatures suggest that not enough heat is conducted through the snow layer even when using a snow thermal conductivity as large as 0.50 $Wm^{-1} K^{-1}$ (value derived from observed snow and ice internal temperature profiles). A surface energy budget of simulated and observed energy fluxes confirms this finding.

Citation: Huwald, H., L.-B. Tremblay, and H. Blatter (2005), A multilayer sigma-coordinate thermodynamic sea ice model: Validation against Surface Heat Budget of the Arctic Ocean (SHEBA)/Sea Ice Model Intercomparison Project Part 2 (SIMIP2) data, *J. Geophys. Res.*, *110*, C05010, doi:10.1029/2004JC002328.

1. Introduction

[2] The sea ice cover in polar regions has an important influence on the high-latitude surface energy budget, and consequently on the high-latitude and global climate [*Donn and Shaw*, 1966; *Budyko*, 1972; *Walsh*, 1983]. Its high reflectivity as well as insulating properties substantially modify the heat, moisture and momentum exchange between the ocean and the atmosphere. The ice does affect the mixing processes in the ocean surface waters due to salt rejection during ice formation and freshwater release during ice melt. When a snow cover is present, the albedo and insulating effects of the surface are further enhanced [e.g., *Untersteiner*, 1961; *Fichefet and Maqueda*, 1997, 1999]. The thickness of the snow cover in turn significantly influences the thermodynamic evolution of the sea ice. In order to get a realistic representation of the high-latitude climate and climate variability, models must be able to represent adequately the thermodynamic evolution of the snow-ice system.

[1]Now at Environmental Fluid Mechanics Laboratory, Ecole Polytechnique Federale de Lausanne, Lausanne, Switzerland.

0148-0227/05/2004JC002328$09.00

[3] To simulate the sea ice-atmosphere interaction in a realistic way, a model that properly resolves the temporal evolution of the internal ice temperature profile associated with relatively fast changes in forcing is required [*Hanesiak et al.*, 1999; *Ukita and Martinson*, 2001]. Since the response of snow and ice is relatively slow (from hours to months depending on the snow or ice thickness) in comparison with changes in the atmospheric forcing, thermal inertia of the thermal system must be considered to properly simulate the snow and ice internal temperature profiles, the basal ice growth, the onset of melt, the ablation rate, and even the breakup date for the ice pack.

[4] The multilayer thermodynamic sea ice model of *Maykut and Untersteiner* [1971] (hereinafter referred to as MU71) computes the temporal variation of the internal temperature within the snow and ice layers, including internal heating due to penetrating shortwave radiation and heat storage in brine pockets. The effect of brine is parameterized using the temperature- and salinity-dependent heat conductivity and specific heat capacity. However, the model does not take into account the dependency of the effective latent heat of fusion on the temperature and salinity which determines the energy of melt. The zero-layer thermodynamic model of *Semtner* [1976] is a simplification of the multilayer model of MU71. The model assumes that the ice has no heat capacity, uses fixed values of thermal conductivity and heat capacity, ignores the internal heating, and allows for the simple calculation of the ice/snow surface temperature and the rate of thickness change from two piecewise linear temperature profiles. The main purpose of these simplifications was to develop a numerically efficient sea ice model to be used in large-scale climate simulations. The thermodynamic sea ice model of *Semtner* [1976], or some variations of it, is used in several earlier large-scale simulations including the Arctic and its subsystems [e.g., *Parkinson and Washington*, 1979; *Mellor and Kantha*, 1989; *Bitz et al.*, 1996].

[5] In many recent studies, various parameterizations of physical processes such as the surface albedo, radiative and turbulent heat fluxes, ocean heat flux, meltwater ponds, and lead fraction were introduced. In these models, the snow sea ice system was coupled to more or less complex models of the ocean mixed layer or the planetary boundary layer. For instance, the model of *Gabison* [1987] describes an extension of the MU71 model with special focus on ocean-atmosphere interaction. This model includes a complex mixed layer ocean model and parameterizations of the surface albedo, radiative and turbulent heat fluxes. Later, *Cox and Weeks* [1988] focused on the thermal impact of brine pockets trapped in the ice. They propose parameterizations of salt entrapment, brine expulsion and drainage due to gravity. *Björk* [1992] adopts the MU71 expression for the ice thermal conductivity and considers the effect of brine pockets by introducing a formulation for the temperature- and salinity-dependent latent heat of fusion while using an expression for the specific heat similar to that proposed in MU71. The specific and latent heat are function of the brine fraction which reduces the amount of energy required for ice melt.

[6] *Ebert and Curry* [1993] presented a one-dimensional thermodynamic model based on MU71. This model also includes parameterizations of meltwater ponds, leads, ocean heat flux, turbulent heat fluxes and the surface albedo. In their model, however, sea ice-atmosphere feedbacks are not explicitly considered since precipitation, radiative fluxes, air temperature, humidity and wind speed are prescribed. To simulate the climate sensitivity of landfast Arctic sea ice, *Flato and Brown* [1996] use a thermodynamic model which is coupled to a simple mixed layer. Their model employs an albedo parameterization different to that of *Ebert and Curry* [1993], and does not consider meltwater ponds. *Launiainen and Cheng* [1998] presented a one-dimensional thermodynamic model which is coupled to an atmospheric boundary layer model allowing for ice-atmosphere interactions. Particular focus is on the parameterization of radiative and turbulent heat fluxes which account for the ice-atmosphere feedbacks. They also provide a nice summary of most thermodynamic sea ice models published prior to their study.

[7] *Bitz and Lipscomb* [1999] introduce an energy-conserving thermodynamic sea ice model in which the internal temperature and brine pocket evolution are coupled. In this model, the latent heat of fusion, the heat capacity and the thermal conductivity depend on the salinity and temperature of the ice. Considering the effect of brine leads to a larger heat capacity but smaller energy of melt since ice continuously melts (brine fraction increases) as the internal temperature increases. Most previous models did not account for the salinity dependence of the latent heat of fusion and consequently do not strictly conserve energy. Finally, *Ukita and Martinson* [2001] present a thermodynamic sea ice model in which the minimum number of layers required to properly define the internal temperature evolution is calculated every time step. In this model, the layer thicknesses are such that a thermal equilibrium can be reached in one time step for a given forcing frequency and thermal conduction in the snow or ice. The number of layers in the ice and snow is no longer fixed which can be an advantage for numerical efficiency. Most of these previous models however prescribe a salinity profile with fixed salinity at the ice surface and base. Consequently, an implied redistribution of salt (addition or loss) is present when the ice base or surface melts, or when the ice base grows.

[8] In this study, a one-dimensional multilayer sigma-coordinate thermodynamic sea ice model is presented. The model includes penetrating shortwave radiation- and temperature-dependent material properties such as thermal conductivity, heat capacity and latent heat of fusion to account for brine pockets and the associated internal storage of heat [*Bitz and Lipscomb*, 1999]. The model considers an arbitrary fixed number of layers within the snow and ice. A coordinate transformation (novel for sea ice thermodynamic models) allows for automatic relayering associated with changes in ice and snow thickness in an energy-conserving manner. This is achieved through an advection term which naturally appears in the transformed energy equation. The model includes all relevant one-dimensional physics of previous thermodynamic models while introducing a more natural framework and easier handling of numerics when compared to previous models. It also conserves the total energy in a given layer (Jm^{-2}) which takes into account

variations in internal energy when changes in ice or snow thickness are present.

[9] The simulation results presented in this study are also a contribution to the Sea Ice Model Intercomparison Project, Part 2, Thermodynamics (SIMIP2) (http://acsys.seos.uvic.ca/acsys/simip2). SIMIP2 is a joint initiative of the World Climate Research Program (Arctic Climate System Study/Climate and Cryosphere–Numerical Experimentation Group), and the Global Energy and Water Cycle Experiment (Cloud System Study/Working Group on Polar Clouds). Its goal is to evaluate and improve the representation of sea ice thermodynamic processes in climate models. This is done by assessing the ability of various thermodynamic sea ice models to predict the sea ice thickness temporal evolution when forced with observational data derived from the Surface Heat Balance of the Arctic Ocean (SHEBA) project. Since the same ice thickness temporal evolution at a given point can be achieved in a number of ways (i.e., using different combinations of snow depth, snow thermal conductivity, ocean heat flux, etc.), additional validation data are required to better constrain the problem. In a companion paper, *Huwald et al.* [2005] present a detailed analysis of the SHEBA data and propose a consistent forcing and validation data set for this comparison. A short summary of the main findings from *Huwald et al.* [2005] is given in section 3.

[10] In this study, the multilayer sigma-coordinate thermodynamic sea ice model is tested against the original SIMIP2 data set and the data set proposed in the companion paper. Sensitivity analyses motivated by the findings from *Huwald et al.* [2005] are also presented to assess both the accuracy of the model simulations and the self-consistency of the SHEBA observations. In summary, the three main goals of this paper are the introduction of a sigma-coordinate thermodynamic sea ice model, the validation of this model against SIMIP2 data, and an evaluation of the data set proposed by *Huwald et al.* [2005] based on a sensitivity analysis of the model results.

[11] The outline of the paper is as follows: section 2 presents the thermodynamic sea ice model, including a description of the numerical scheme used to solve the resulting governing equations. An overview of the SHEBA data used to force and validate the model is given in section 3. Section 4 presents a discussion of the simulation results and a comparison with SHEBA/SIMIP2 data including sensitivity experiments and a surface energy budget. The main conclusions drawn from the simulation results are summarized in section 5.

2. Sea Ice Thermodynamic Model

[12] A sigma-coordinate one-dimensional multilayer thermodynamic sea ice model is presented. The conservation of energy equation (including penetrating shortwave radiation) is used to describe the temperature evolution in the snow and ice. Brine pockets in the ice are parameterized using a temperature- and salinity-dependent heat capacity, thermal conductivity, and latent heat of fusion following MU71 and *Bitz and Lipscomb* [1999]. Equations are written in terrain-following (sigma-)coordinates. This allows for automatic relayering and redistribution of energy between the layers in an energy-conserving manner. The model allows for an arbitrary fixed number of layers in the snow and ice slabs and therefore for a proper representation of the internal temperature profile under fast changing atmospheric conditions.

[13] The time required to reach thermal equilibrium in a material layer of thickness Δz is given by the diffusive timescale $\tau_d = \rho c_p (\Delta z)^2/k$, where k is the thermal conductivity, ρ is the density, and c_p is the specific heat capacity of snow or ice. For instance, for a snow and ice layer thickness of 0.2 m and 3 m, the thermal inertia can be neglected when the forcing has periods greater than 1 day and 3 months respectively. Conversely, the layer thickness required to resolve changes in surface forcing with a period t_f is $\Delta z = (t_f \rho c_p/k)^{0.5}$.

[14] Lateral thermodynamic and dynamic effects such as horizontal conduction and horizontal advection of ice are not considered. The model is Lagrangian in nature and describes the thermodynamic evolution of a vertical line at a fixed point on a sea ice floe (e.g., SHEBA). In the following, fluxes toward a given surface are defined positive. A list of parameters and physical constants (and their numerical value) appearing in the following equations is given in Table 1.

2.1. Model Equations

[15] The prognostic variables in this model are the snow/ice thickness (h) and the internal snow/ice temperature (T, in Celsius). The one-dimensional conservation of mass equation for snow and ice can be written as

$$\frac{\partial h}{\partial t} = S_h \ , \tag{1}$$

where h is the snow or ice thickness, t denotes time, and S_h is a thermodynamic source term. Rewriting equation (1) in terms of the snow/ice surface and base elevations (see Figure 1), we obtain (fluxes toward the surface are positive)

$$\frac{\partial s_s}{\partial t} = -\left(F_{net} + F_{cs}\right)/\left(\rho_s L_f\right) \ , \ \text{if } F_{net} + F_{cs} > 0 \\ + p \cdot \rho_w/\rho_s \ , \ \text{if } T_a \le 0^\circ\text{C}, \tag{2}$$

$$\frac{\partial s_i}{\partial t} = \begin{cases} -\left(F_{net} + F_{cs}\right)/\left(\rho_i L_f\right) \ , & \text{if } F_{net} + F_{cs} > 0 \\ 0 \ , & \text{if } F_{net} + F_{cs} = 0 \end{cases}, \tag{3}$$

$$\frac{\partial b_i}{\partial t} = \frac{F_{ocn} + F_{cb}}{\rho_i L_f}, \tag{4}$$

where s and b are the surface and base elevations, the subscripts "s" and "i" stand for snow and ice, p is a precipitation rate given in snow water equivalent, ρ_i, ρ_s and ρ_w are the density of ice, snow and freshwater, T_a is the air temperature, F_{cs} and F_{cb} are the conductive heat fluxes at the snow/ice surface and ice base, F_{ocn} is the ocean heat flux at the ice base, L_f is the specific latent heat of fusion, and F_{net} is the net atmospheric heat flux at the surface, defined as

$$F_{net} = \epsilon\left(F_{lw} - \sigma(T_{surf} + T_0)^4\right) + (1-\alpha)(1-i_0)F_{sw} \\ + F_{sh} + F_{lh} + F_P, \tag{5}$$

Table 1. Physical Parameters and Constants Used in the Model

Symbol	Variable or Constant Name	Value	Unit
β	empirical constant (equation (20))	0.1172	Wm^{-1} psu^{-1}
C_{sh}	sensible heat transfer coefficient	1.0×10^{-3}	
C_{lh}	latent heat transfer coefficient	1.0×10^{-3}	
c_{pa}	heat capacity of air	1.01×10^{3}	J kg^{-1} K^{-1}
c_{p0}	heat capacity of freshwater ice or snow	2.06×10^{3}	J kg^{-1} K^{-1}
c_{po}	heat capacity of ocean water at 30 psu	3.99×10^{3}	J kg^{-1} K^{-1}
c_{pw}	heat capacity of water	4.17×10^{3}	J kg^{-1} K^{-1}
c_1	empirical constant (equation (10)) (ice, water)	21.87, 17.27	
c_2	empirical constant (equation (10)) (ice, water)	7.66, 35.86	
ϵ	emissivity of ice, snow	0.99	
γ	empirical constant (equation (21))	1.8×10^{4}	J °C kg^{-1} psu^{-1}
k_s	thermal conductivity of snow	0.31	Wm^{-1} K^{-1}
k_{i0}	thermal conductivity of freshwater ice	2.03	Wm^{-1} K^{-1}
κ_i	bulk extinction coefficient of ice	1.5	m^{-1}
κ_s	bulk extinction coefficient of snow	10	m^{-1}
L_{f0}	latent heat of fusion of freshwater ice	3.34×10^{5}	J kg^{-1}
L_s	latent heat of sublimation	2.83×10^{6}	J kg^{-1}
μ	empirical constant (equation (15))	0.054	°C psu^{-1}
P_{surf}	surface air pressure	1013.25	hPa
ρ_a	density of air	1.28	kg m^{-3}
ρ_s	density of snow	330	kg m^{-3}
ρ_i	density of freshwater ice	917	kg m^{-3}
ρ_o	density of ocean water at 30 psu	1025	kg m^{-3}
ρ_w	density of freshwater	1000	kg m^{-3}
σ	Stefan-Boltzmann constant	5.67×10^{-8}	Wm^{-2} K^{-4}
S_o	salinity of surface ocean water	29.6	psu
S_b	salinity of newly formed basal sea ice	10.0	psu
T_0	freezing temperature of freshwater	273.16	K
i_0	fraction of net shortwave radiation penetrating the snow or ice surface	0.08, 0.15	

where

$$F_{sh} = \rho_a \, c_{pa} \, C_{sh} \, |\mathbf{u}_a| \, (T_a - T_{surf}) \, , \tag{6}$$

$$F_{lh} = \rho_a \, L_s \, C_{lh} \, |\mathbf{u}_a| \, (q_a - q_{surf}) \, , \tag{7}$$

$$F_P = p \, \rho_w c_{pw} \max(T_a - T_{surf}, \, 0) \, , \tag{8}$$

ϵ is the surface emissivity, F_{lw} and F_{sw} are the downward longwave and shortwave radiation, σ is the Stefan-Boltzmann constant, T_{surf} is the surface temperature in Celsius, T_0 is the zero Celsius reference temperature in Kelvin, α is the albedo, i_0 is the surface transmission coefficient (different for snow and ice), F_{sh} and F_{lh} are the sensible and latent heat flux, F_P is the energy input associated with warm rain falling on the snow or ice surface, c_{pw} is the heat capacity of freshwater, ρ_a, c_{pa}, $\mathbf{u}_a$ and q_a are the density, heat capacity, velocity, and specific humidity of air, L_s is the specific latent heat of sublimation, and C_{sh} and C_{lh} are the sensible and latent heat transfer coefficients. The specific humidity at the snow or ice surface (q_{surf}) is assumed to be at saturation and is computed according to

$$q_{surf} = \frac{0.622 \, e_s}{P_{surf} - 0.378 \, e_s} \, , \tag{9}$$

where P_{surf} is the surface air pressure and e_s is the saturation vapor pressure calculated as [*Murray*, 1967]

$$e_s = 6.11 \cdot \exp\left(\frac{c_1 \, T_{surf}}{T_{surf} + T_0 - c_2}\right), \tag{10}$$

where c_1 and c_2 are constant coefficients (defined in Table 1).

[16] The internal snow and ice temperature is described by the one-dimensional heat conduction equation

$$\rho \frac{\partial E}{\partial t} = \rho \left(\frac{\partial E}{\partial T} \frac{\partial T}{\partial t} + \frac{\partial E}{\partial S} \frac{\partial S}{\partial t} \right) = - \frac{\partial F_c}{\partial z} + R, \tag{11}$$

where E is the internal energy of the sea ice brine mixture, T, S are the internal snow or ice temperature and salinity, $F_c = -k \, (\partial T / \partial z)$ is the conductive heat flux in the snow or

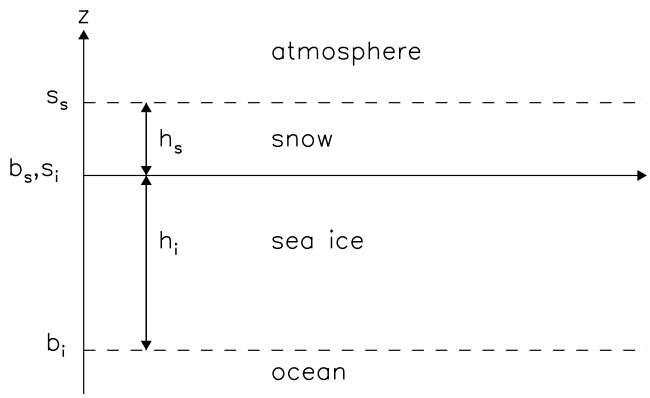

Figure 1. Sea ice thermodynamic model schematic. The letters "s" and "b" denote the surface and base, subscripts "s" and "i" stand for snow and ice, and h_s and h_i are the snow and ice thickness (positive numbers), respectively. The z coordinate is positive upward.

ice, and R is the absorbed shortwave energy per unit volume, defined as

$$R = \begin{cases} F_{\mathrm{ps}}\,\kappa_{\mathrm{s}}\,e^{-\kappa_{\mathrm{s}}(s_{\mathrm{s}}-z)}, & \text{for } b_{\mathrm{s}} < z < s_{\mathrm{s}} \\ F_{\mathrm{pi}}\,\kappa_{\mathrm{i}}\,e^{-\kappa_{\mathrm{i}}(s_{\mathrm{i}}-z)}, & \text{for } b_{\mathrm{i}} < z < s_{\mathrm{i}} \end{cases}, \tag{12}$$

where

$$\begin{aligned} F_{\mathrm{ps}} &= F_{\mathrm{sw}}(1-\alpha)i_0 \quad \text{at the snow or ice surface,} \\ F_{\mathrm{pi}} &= F_{\mathrm{ps}}\,e^{-\kappa_{\mathrm{s}}h_{\mathrm{s}}}, \quad \text{at the snow-ice interface,} \end{aligned} \tag{13}$$

κ_{s} and κ_{i} are the extinction coefficient for snow and ice, and F_{ps} and F_{pi} are the shortwave radiation penetrating the snow and ice surface respectively (following Beer's Law). At the surface, the incident shortwave radiation F_{sw} is split into three parts: a reflected part αF_{sw}, a fraction absorbed directly at the surface $(1-\alpha)(1-i_0)F_{\mathrm{sw}}$, and a part penetrating into the snow or ice $(1-\alpha)i_0F_{\mathrm{sw}}$.

[17] Since the salinity of sea ice changes on much larger timescales compared to the internal snow/ice temperature, the time derivative $\partial S/\partial t$ in equation (11) is considered equal to zero. In this case, equation (11) reduces to

$$\begin{aligned} \rho\frac{\partial E}{\partial t} &= \rho\left(\frac{\partial E}{\partial T}\frac{\partial T}{\partial t}+\frac{\partial E}{\partial S}\frac{\partial S}{\partial t}\right) \\ &= \rho c_p\frac{\partial T}{\partial t} = -\frac{\partial F_{\mathrm{c}}}{\partial z}+R. \end{aligned} \tag{14}$$

This is an implicit assumption made in most existing thermodynamic models which solve for this equation. In the following, we will work with equation (11) considering $\partial S/\partial t = 0$.

2.2. Boundary Conditions

[18] At the ice base, the temperature T is set to the ocean freezing temperature:

$$T(z = b_{\mathrm{i}}, t) = T_{\mathrm{f}}(S) = -\mu S_{\mathrm{o}}, \tag{15}$$

where $T_{\mathrm{f}}(S)$ is the salinity-dependent freezing point temperature of water, μ is an empirical constant equal to $0.054^{\circ}\mathrm{C\ psu^{-1}}$ and S_{o} is the ocean surface salinity. At the snow-ice interface, the temperature and the conductive heat flux in the snow ($z = b_{\mathrm{s}}$) and ice ($z = s_{\mathrm{i}}$) are equal:

$$T_{\mathrm{s}}(z = b_{\mathrm{s}}, t) = T_{\mathrm{i}}(z = s_{\mathrm{i}}, t) \tag{16}$$

$$-k_{\mathrm{s}}\left.\frac{\partial T_{\mathrm{s}}}{\partial z}\right|_{z=b_{\mathrm{s}}} = -k_{\mathrm{i}}\left.\frac{\partial T_{\mathrm{i}}}{\partial z}\right|_{z=s_{\mathrm{i}}}. \tag{17}$$

At the surface, the conductive heat flux in the snow (or in the ice if snow is not present), is set equal to the net atmospheric heat flux. If this results in a surface temperature T_{surf} which is above the freezing point, T_{surf} is set to T_{f} and the residual heat imbalance is used for melting, i.e.,

$$-k\left.\frac{\partial T}{\partial z}\right|_{z=s} = F_{\mathrm{net}}, \qquad \text{for } T_{\mathrm{surf}} < T_{\mathrm{f}}(S) \tag{18}$$

$$T(z = s, t) = T_{\mathrm{f}}(S), \qquad \text{otherwise.} \tag{19}$$

2.3. Brine Pocket Parameterization

[19] The brine pocket parameterization accounts for the temperature and salinity dependence of the sea ice properties. The parameterization used in this model follows MU71 and *Bitz and Lipscomb* [1999]. The matrix of sea ice is assumed to consist of freshwater ice and a complex system of cavities of various shapes such as cracks, fractures and pockets. Below the freeboard, these cavities are usually filled with a brine solution; above they can contain air, brine or low-salinity meltwater originating from the ice surface. At equilibrium, the temperature of the liquid brine pockets (T_{b}) must be at freezing and equal to the ice temperature, i.e., $T_{\mathrm{b}} = T_{\mathrm{i}} = -\mu S_{\mathrm{b}}$, where S_{b} is the salinity of the salt water solution in the pocket (grams of salt per kg of water). If not, the brine pocket would grow or reduce its size thereby adjusting its salinity in such a way that T_{b} would be equal to the ice temperature T_{i} [*Schwerdtfeger*, 1963]. The brine salinity (S_{b}) can be related to the mean salinity of the ice (S_{i}) by $S_{\mathrm{b}}M_{\mathrm{b}} = S_{\mathrm{i}}\,(M_{\mathrm{b}} + M_{\mathrm{i}})$ where M_{b} and M_{i} are the mass of brine and ice respectively. The mass fraction of brine f_b can be written as $M_{\mathrm{b}}/(M_{\mathrm{b}} + M_{\mathrm{i}}) = S_{\mathrm{i}}/S_{\mathrm{b}} = -\mu S_{\mathrm{i}}/T_{\mathrm{i}}$. Brine pockets are parameterized by approximating the heat capacity of an ice layer as a function of temperature and salinity. Also the bulk thermal conductivity varies with temperature and salinity. Such functions were first introduced by *Untersteiner* [1961]:

$$k_{\mathrm{i}}(S, T) = k_{\mathrm{i}0} + \frac{\beta S_{\mathrm{i}}}{T_{\mathrm{i}}} \tag{20}$$

$$c_p(S, T) = c_{p0} + \frac{\gamma S_{\mathrm{i}}}{T_{\mathrm{i}}^2}, \tag{21}$$

where $k_{\mathrm{i}0}$ and c_{p0} are the thermal conductivity and specific heat capacity of ice with zero salinity, β is a constant equal to 0.1172 $\mathrm{Wm^{-1}\ psu^{-1}}$, c_p is the specific heat capacity of the ice-brine mixture and γ is a constant equal to 1.8×10^4 J °C $\mathrm{kg^{-1}\ psu^{-1}}$.

[20] In a later work, *Ono* [1967] showed that the temperature and salinity dependency of the heat capacity in equation (21) can be derived from first principles. The internal energy of the sea ice brine mixture (E) can be written as [*Schmidt et al.*, 2004]

$$E = c_{p0}\left(1-\underbrace{\frac{-\mu S_{\mathrm{i}}}{T_{\mathrm{i}}}}_{f_b}\right)T_{\mathrm{i}} - L_{f0}\left(1-\underbrace{\frac{-\mu S_{\mathrm{i}}}{T_{\mathrm{i}}}}_{f_b}\right) + c_{p\mathrm{o}}\underbrace{\frac{-\mu S_{\mathrm{i}}}{T_{\mathrm{i}}}}_{f_b}T_{\mathrm{i}}, \tag{22}$$

where L_{f0} is the specific latent heat of fusion of pure ice and $c_{p\mathrm{o}}$ is the specific heat capacity of ocean water. The specific heat capacity of saline sea ice $c_p = \partial E/\partial T_{\mathrm{i}}$ can then be expressed as

$$c_p = c_{p0} + \frac{\gamma S_{\mathrm{i}}}{T_{\mathrm{i}}^2}, \tag{23}$$

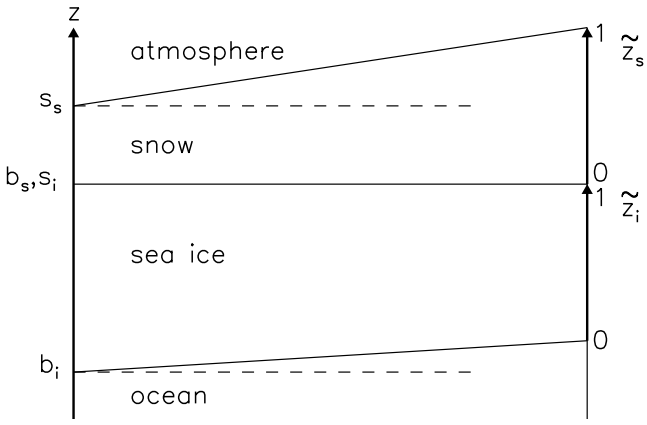

Figure 2. Coordinate transformation of the snow and ice components.

where $\gamma = \mu L_{f0}$. The amount of energy required to melt a unit mass of ice of a given temperature and salinity in turn can be expressed as

$$\begin{aligned} L_f(S,T) &= -c_{p0}T_{\mathrm{i}}\left(1+\frac{\mu S_{\mathrm{i}}}{T_{\mathrm{i}}}\right)+L_{f0}\left(1+\frac{\mu S_{\mathrm{i}}}{T_{\mathrm{i}}}\right) \\ &\quad + c_{po}\frac{\mu S_{\mathrm{i}}}{T_{\mathrm{i}}}T_{\mathrm{i}} - c_{po}\mu S_{\mathrm{i}} \\ &= c_{p0}(T_{\mathrm{f}}-T_{\mathrm{i}})+L_{f0}\left(1+\frac{\mu S_{\mathrm{i}}}{T_{\mathrm{i}}}\right). \end{aligned} \tag{24}$$

The first term on the right hand side of equation (24) is the energy needed to bring the fresh ice fraction from temperature T_{i} to the freezing point temperature 0°C; the second term is the amount of energy required to melt the fresh ice fraction; the third term is the energy required to bring the brine fraction $(-\mu S_{\mathrm{i}}/T_{\mathrm{i}})$ from T_{i} to 0°C and the fourth term is the energy needed to bring the total brine mixture (of salinity S_{i}) to its freezing point temperature T_{f} $(=-\mu S_{\mathrm{i}})$. For an ocean freezing temperature of −1.6°C (corresponding to an ocean water salinity of 29.6 psu) and a bulk sea ice salinity of 4 psu, L_{f0} is reduced by 13% ($L_f = 0.87L_{f0}$).

2.4. Coordinate Transformation

[21] Terrain-following coordinates were first used in weather forecasting models by *Phillips* [1957] and later in the field of ice sheet modeling by *Jenssen* [1977]. *Hindmarsh and Hutter* [1988] elaborate on the mathematical background of the transformation. For sea ice, this method has not yet been documented in the literature although some groups are using similar techniques in the sea ice component of their climate models (e.g., NASA-GISS). The advantage of the coordinate transformation is the natural handling of relayering associated with melting and freezing of sea ice and melting and accumulation of snow. To this end, a coordinate transformation is introduced with the base and surface positioned at $\tilde{z} = 0$ and $\tilde{z} = 1$ (Figure 2):

$$\tilde{z} = \frac{z-b}{s-b}, \tag{25}$$

where s and b are equal to s_{s} and b_{s} for the snow layer and s_{i} and b_{i} for the ice layer. In the new coordinate system, $\tilde{z}$ is positive upward and the snow and ice base are located at $\tilde{z} = 0$.

[22] Using the chain rule of differentiation, equation (11) can be rewritten in terms of the transformed coordinate $\tilde{z}$ as (transformed variables are marked with tilde)

$$\rho\left(\frac{\partial\tilde{E}}{\partial\tilde{t}}+\tilde{w}\frac{\partial\tilde{E}}{\partial\tilde{z}}\right)=\frac{1}{h^2}\frac{\partial}{\partial\tilde{z}}\left(k\frac{\partial\tilde{T}}{\partial\tilde{z}}\right)+\tilde{R}, \tag{26}$$

where $h = s - b$ and (using equation (25))

$$\tilde{w}=\frac{\partial\tilde{z}}{\partial\tilde{t}}=-\frac{(1-\tilde{z})}{h}\frac{\partial b}{\partial t}-\frac{\tilde{z}}{h}\frac{\partial s}{\partial t}. \tag{27}$$

In the above, the transformation equation for time is $\tilde{t} = t$. The tilde notation is used here for consistency reasons. The continuity equation (equation (1)) is not a function of $\tilde{z}$ and remains the same in transformed coordinates.

[23] Multiplying equation (26) by h and equation (1) by $\rho\tilde{E}$ and adding yields the energy equation in a flux form where the total energy of one layer is conserved:

$$\begin{aligned} &\rho\left(h\frac{\partial\tilde{E}}{\partial\tilde{t}}+\tilde{E}\frac{\partial h}{\partial\tilde{t}}+\frac{\partial(\tilde{w}h\tilde{E})}{\partial\tilde{z}}\right)-\rho\tilde{E}\frac{\partial(\tilde{w}h)}{\partial\tilde{z}} \\ &\quad=\frac{1}{h^2}\frac{\partial}{\partial\tilde{z}}\left(k\frac{\partial(h\tilde{T})}{\partial\tilde{z}}\right)+h\tilde{R}+\rho\tilde{E}S_h. \end{aligned} \tag{28}$$

The thickness h is not function of $\tilde{z}$ and is taken into the argument of the differential operator for the advective and the diffusive terms. From equation (27),

$$\frac{\partial(\tilde{w}h)}{\partial\tilde{z}}=\frac{\partial b}{\partial\tilde{t}}-\frac{\partial s}{\partial\tilde{t}}=-\frac{\partial h}{\partial\tilde{t}}. \tag{29}$$

Substituting equation (29) into equation (28), and using the continuity equation (equation (1)), leads to the final form of the transformed energy equations for snow and ice:

$$\rho\left(\frac{\partial(h_{\mathrm{s}}\tilde{E}_{\mathrm{s}})}{\partial\tilde{t}}+\frac{\partial(\tilde{w}_{\mathrm{s}}h_{\mathrm{s}}\tilde{E}_{\mathrm{s}})}{\partial\tilde{z}_{\mathrm{s}}}\right)=\frac{1}{h_{\mathrm{s}}^2}\frac{\partial}{\partial\tilde{z}_{\mathrm{s}}}\left(k_{\mathrm{s}}\frac{\partial\tilde{\theta}_{\mathrm{s}}}{\partial\tilde{z}_{\mathrm{s}}}\right)+h_{\mathrm{s}}\tilde{R}\ , \quad \text{for } 0<\tilde{z}_{\mathrm{s}}<1 \tag{30}$$

$$\rho\left(\frac{\partial(h_{\mathrm{i}}\tilde{E}_{\mathrm{i}})}{\partial\tilde{t}}+\frac{\partial(\tilde{w}_{\mathrm{i}}h_{\mathrm{i}}\tilde{E}_{\mathrm{i}})}{\partial\tilde{z}_{\mathrm{i}}}\right)=\frac{1}{h_{\mathrm{i}}^2}\frac{\partial}{\partial\tilde{z}_{\mathrm{i}}}\left(k_{\mathrm{i}}\frac{\partial\tilde{\theta}_{\mathrm{i}}}{\partial\tilde{z}_{\mathrm{i}}}\right)+h_{\mathrm{i}}\tilde{R}, \quad \text{for } 0<\tilde{z}_{\mathrm{i}}<1 \tag{31}$$

where $h\tilde{E}$ is the total internal energy of a given layer (to within a constant) and $\tilde{\theta} = h\tilde{T}$. The transformation introduces an additional advection term in the heat conduction equation which naturally takes into account the energy transport from one layer to the next associated with relayering, when the ice or snow thickness is changing.

[24] Finally, the boundary conditions (equations (15)–(19)) can be rewritten in terms of $\tilde{\theta} = h\tilde{T}$ and the transformed coordinate $\tilde{z}$ as

Ice base

$$\tilde{\theta}(\tilde{z}_{\mathrm{i}}=0,t)=\theta_{\mathrm{f}}(S)=-\mu S_{\mathrm{o}}h_{\mathrm{i}}\ , \tag{32}$$

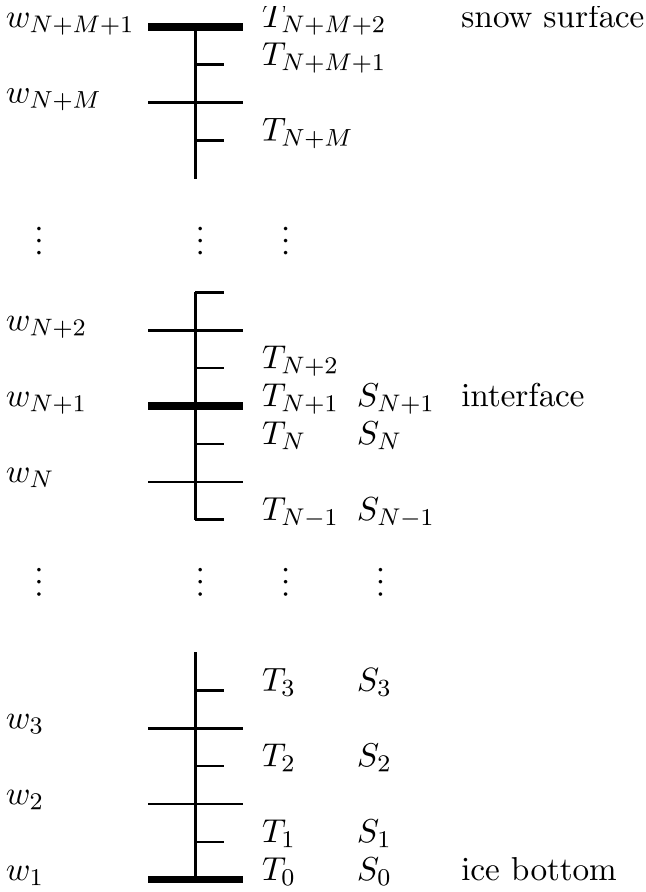

Figure 3. Numerical grid schematic. N and M are the number ice and snow layers, respectively. The vertical velocity component w is defined at the nodes of the grid, and the temperature T and the salinity S are defined at the center of the grid (C-grid). Three additional temperatures and salinities are defined at the surface, the base, and the snow-ice interface.

Snow-ice interface

$$h_i\tilde{\theta}_s(\tilde{z}_s = 0, t) = h_s\tilde{\theta}_i(\tilde{z}_i = 1, t) \tag{33}$$

$$-\frac{k_s}{h_s^2}\frac{\partial\tilde{\theta}_s}{\partial\tilde{z}_s}\bigg|_{\tilde{z}_s=0} = -\frac{k_i}{h_i^2}\frac{\partial\tilde{\theta}_i}{\partial\tilde{z}_i}\bigg|_{\tilde{z}_i=1} \tag{34}$$

Snow or ice surface

$$-\frac{k}{h^2}\frac{\partial\tilde{\theta}}{\partial\tilde{z}}\bigg|_{\tilde{z}=1} = F_{net} \qquad \text{for } \theta_{surf} < \theta_f(S) \tag{35}$$

$$\tilde{\theta}(\tilde{z} = 1, t) = \theta_f(S) \qquad \text{otherwise.} \tag{36}$$

The radiative source term (equation (12)) is transformed by substituting z from equation (25) in equation (12):

$$\tilde{R} = \begin{cases} F_{ps}\,\kappa_s\, e^{-\kappa_s(1-\tilde{z}_s)h_s}, & 0 < \tilde{z}_s < 1 \\ F_{pi}\,\kappa_i\, e^{-\kappa_i(1-\tilde{z}_i)h_i}, & 0 < \tilde{z}_i < 1 \end{cases}. \tag{37}$$

2.5. Numerical Scheme

[25] The heat conduction equation is integrated using a forward in time finite difference numerical scheme. Fluxes and the vertical velocities are defined on the nodes of the grid; temperatures and salinities are located at the center of the grid and hence represent the mean quantity of a grid cell. Three additional temperatures are defined at the ice base, the snow-ice interface, and the snow surface (Figure 3) which are always represented by a grid point owing to the coordinate transformation. The diffusion term is evaluated implicitly, applying a second-order centered in space difference scheme. The advection term $(\partial(\tilde{w}\tilde{\theta})/\partial\tilde{z})$ which accounts for the redistribution of energy from one layer to another, is also evaluated implicitly using a first-order upstream discretization. The snow or ice thickness, the vertical velocities w, the temperature- and salinity-dependent ice properties (k_i, L_f), and surface fluxes are updated using a relaxation method until the temperatures converge. This way, the continuity equation and the transformed energy equation are stepped forward in time implicitly and the resulting internal temperature profile gives conductive heat fluxes that are consistent with the internal energy change of a given layer. The conductive heat fluxes at the surface, base, and snow-ice interface are evaluated using a second-order one-sided difference scheme.

[26] The snow depth can be specified or calculated from observed precipitation rates which are converted to a snow depth using a reference snow density. When the snow depth decreases below a threshold value of 5 cm, only one snow layer is used with a linear temperature profile and zero heat capacity. This is justified when considering the diffusive timescale for hourly varying forcing such as that provided by SIMIP2. The turbulent heat fluxes can be specified from measurements or calculated from standard bulk formulations (equations (6) and (7)) using wind speed, air temperature, and specific humidity. If the bulk formulations are used, the sensible heat flux is evaluated implicitly whereas the saturation vapor pressure in the equation of the latent heat flux is calculated based on the temperature of the previous iteration.

[27] In summer, the surface ablation is always calculated from the energy surplus in a given time step. If the surface temperature T_{surf} exceeds the freezing temperature T_f, the temperature profile is recalculated with T_{surf} fixed at T_f and the amount of surface melt is computed from the resulting imbalance of the net atmospheric and the surface conductive heat flux. Owing to the brine pocket parameterization, internal heating leads to enlargement of the brine pockets and an associated reduction of their salinity while the freezing temperature of the ice is never exactly reached until all ice is melted.

3. Surface Heat Budget of the Arctic Ocean (SHEBA) Data Description

[28] The snow, ice, atmospheric and oceanic data used to force and validate the model were collected during the SHEBA field experiment in the Beaufort and Chukchi seas from October 1997 to October 1998. Atmospheric data were measured at the meteorological tower of the Atmospheric Surface Flux Group (ASFG) [*Persson et al.*, 2002]. Snow/ice thickness and internal temperature was measured by the

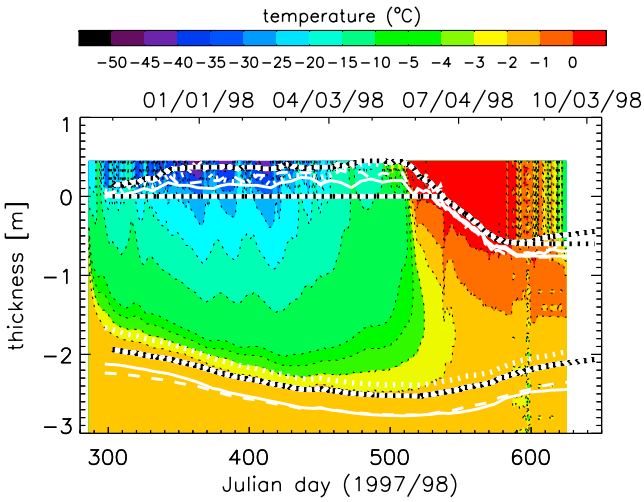

Figure 4. Measured internal ice temperature and thickness evolution from gauges 53 (dashed line), 69 (dotted line), and 71 (solid line) at the mass balance site Pittsburgh. The vertical extent of measurements is defined by the length of the thermistor string. The snow-ice interface is at $z = 0$ during the cold period. As soon as surface melt starts, the ice surface is ablated below $z = 0$. The bold black and white lines denote the best estimates for the snow surface, the snow-ice interface, and the ice base from *Huwald et al.* [2005]. When the snow depth equals zero, the elevation of the snow surface and snow-ice interface are identical and define the ice surface. Julian day zero is defined as 1 January 1997, 0000 LT.

Ice Physics Group (IPG) and are described by *Perovich et al.* [1999], *Perovich and Elder* [2001], and *Sturm et al.* [2002a]. The ocean heat flux was estimated from the growth/melt rate and the internal temperature gradient at the ice base (see *Perovich and Elder* [2002] for details).

[29] For SIMIP2, a subset (31 October 1997–8 October 1998) of the SHEBA data was compiled to initialize, force, and validate the model. These data were taken at the mass balance site "Pittsburgh," located on an undeformed snow covered multiyear ice floe, and include downward radiative fluxes (shortwave and longwave), snow and ice albedo, 10 m wind speed, air temperature and humidity, precipitation (mm d^{-1} snow water equivalent), ocean heat flux, and ice thickness. Measured snow thickness and the internal temperature evolution at the Pittsburgh site (Figure 4), and mean skin temperature measured at the SHEBA sites "Atlanta," "Baltimore," "Florida," and the tower site of the ASFG [*Persson et al.*, 2002] are also used in this study as additional validation data sets. A more detailed description of the data sets mentioned above is provided by *Huwald et al.* [2005].

[30] At Pittsburgh (and other heat balance sites), a thermistor string, extending about a meter below the ice base down into the ocean mixed layer, and up to a few decimeters (depending on snow depth) into the air above the snow or ice surface, measured the internal temperature evolution of the snow and ice, and in the air and upper ocean. Snow and ice thickness was measured with snow stakes and hot wire gauges which were typically arranged at a distance of about one to a few meters around a thermistor string. Most temperature measurements ran from October 1997 to September 1998, providing a record length of almost 11 months. The atmospheric and oceanic forcing fields in SIMIP2, and the snow and ice internal temperature data from the Pittsburgh site are provided with a temporal resolution of one hour. The snow and ice thickness measurements are provided at a lower temporal resolution of 2 days (summer) to 2 weeks (winter).

[31] Since the snow/ice internal temperatures are used to validate the model and since the spatial variability in the snow and ice thickness at SHEBA is large, the exact snow and ice thicknesses at the thermistor string location have to be determined to obtain a consistent ice/snow thickness and internal temperature data set. An analysis of the temporal evolution of the snow/ice internal temperatures and thicknesses by *Huwald et al.* [2005] shows that (1) the initial ice thickness at the exact location of the Pittsburgh thermistor string is 24 cm thicker than the value proposed in SIMIP2 (based on gauge 69), (2) the winter mean snow depth (32 cm) is 6 cm thicker than the corresponding value derived from gauge 69 alone, and 11 cm thicker than the mean snow depth derived from precipitation measurements (and assuming a constant snow density of 330 kg m^{-3}) (the SIMIP2 precipitation rates were multiplied by a factor of 1.5 to account for gauge undercatch), (3) the ocean heat flux at Pittsburgh during spring and summer is generally lower than that provided by SIMIP2 (by 1 Wm^{-2} based on yearly average), and (4) the snow thermal conductivity derived from the continuity of the conductive heat flux at the snow-ice interface is 0.50 Wm^{-1} K^{-1} as opposed to 0.31 Wm^{-1} K^{-1} (as proposed in SIMIP2), or 0.14 Wm^{-1} K^{-1} (value derived from in situ measurements at SHEBA [*Sturm et al.*, 2002b]).

[32] For these reasons, the results presented hereafter will include the original SIMIP2 "control experiment" as well as a series of sensitivity experiments where the ice base, snow depth, ocean heat flux and snow thermal conductivity are modified according to the findings of *Huwald et al.* [2005].

4. Results and Discussion

[33] SIMIP2 considers a simple one-dimensional heat and mass balance on a horizontally homogeneous slab of potentially snow-covered sea ice (i.e., a Lagrangian approach). To this end, such effects as horizontal heat conduction caused by spatial variability in the snow depth or ice thickness are not taken into account. These effects are quantified by *Huwald et al.* [2005] based on results from a two-dimensional steady state heat conduction model.

[34] In the following experiments, the model is forced with specified hourly downwelling shortwave and longwave radiation, turbulent heat fluxes (calculated using standard bulk formulations), 10 m wind speed, air temperature, and humidity. Other prescribed quantities are the precipitation rate, the ocean heat flux at the ice base and the surface albedo. All forcing fields are provided by SIMIP2 and *Huwald et al.* [2005]. All model runs are performed with 10 layers in the ice and in the snow, and with a time step of one hour.

Table 2. Summary of Observed and Simulated Ice Thickness Characteristics at Pittsburgh[a]

Experiment	h_{ini}	h_{max}	h_{min}	g_b	m_s	m_b	m_t
Observation (gauge 69)	1.70	2.40	1.37	0.70	0.60	0.43	1.03
Observation (mean of three gauges)	2.03	2.65	1.54	0.62	0.71	0.40	1.11
Observation (best estimates)	1.94	2.53	1.50	0.59	0.60	0.43	1.03
Experiment 1: ctrl, SIMIP2 IC	1.70	2.33	1.26	0.63	0.53	0.54	1.07
Experiment 2: corrected IC	1.94	2.49	1.41	0.55	0.55	0.53	1.08
Experiment 3: ocean heat flux	1.94	2.66	1.71	0.72	0.57	0.38	0.95
Experiment 4a: snow, gauge 69	1.94	2.55	1.55	0.61	0.60	0.40	1.00
Experiment 4b: snow, mean of three gauges	1.94	2.57	1.55	0.63	0.59	0.41	1.00
Experiment 4c: snow, best estimate	1.94	2.43	1.42	0.49	0.60	0.41	1.01
Experiment 5: $k_s = 0.50$	1.94	2.57	1.56	0.63	0.61	0.40	1.01
Experiment 6: low resolution	1.94	2.56	1.56	0.62	0.60	0.40	1.00

[a]Values in meters. Abbreviations are as follows: h_{ini}, initial ice thickness; h_{max}, maximum ice thickness before melt starts; h_{min}, minimum ice thickness at the end of the melt season; g_b, basal growth; m_s, surface melt; m_b, basal melt; m_t, total ablation. In experiments 1 and 2, IC stands for initial conditions.

[35] Ocean temperatures measured at the lowest thermistor of the Pittsburgh string (3.9 m below the initial snow-ice interface) range from −1.8°C to −1.4°C during the SHEBA year with a mean of −1.6°C. This corresponds to ocean salinity ranging from 33.3 psu to 25.9 psu with a mean of 29.6 psu. SIMIP2 proposes an ocean freezing temperature of −1.96°C, which is lower than the lowest ocean temperature measured at Pittsburgh. In this study, the salinity of the ocean surface waters and the corresponding freezing temperature (equation (15)) are assumed constant in time and equal to 29.6 psu and −1.6°C respectively. Note that simulation results showed that these differences in the ocean freezing temperature have a negligible effect on the evolution of the ice base. The salinity profile in the ice is a linear with 1 psu at the surface and 4 psu at the ice base in accord with *Perovich and Elder* [2002].

[36] After presenting the SIMIP2 control experiment (experiment 1, section 4.1), the sensitivity of the model to initial ice thickness (experiment 2, section 4.1) and ocean heat flux (experiment 3, section 4.2) is investigated. Sections 4.3 and 4.4 elaborate on the effect of the snow depth (experiments 4a–4c) and snow thermal conductivity (experiment 5) on the simulation results. Key characteristics of the simulated and observed ice thickness evolution for all experiments are summarized in Table 2.

4.1. Sea Ice Model Intercomparison Project Part 2 (SIMIP2) Control Experiment

[37] The observed initial conditions (31 October 1997) for the SIMIP2 control experiment (experiment 1) are 5 cm snow depth, 170 cm ice thickness, and internal snow/ice temperature and salinity profiles measured at the SHEBA site Pittsburgh. The snow cover in the control experiment is calculated from specified precipitation rates using a reference snow density of 330 kg m^{-3}. As proposed by SIMIP2, the precipitation rates are increased by 50% from the observed values since they resulted in too low snow thicknesses when compared to snow stake measurements. The reference values of other model parameters used in the control experiment are given in Table 1.

[38] The simulated snow/ice internal temperature and thickness evolutions for the control experiment (Figure 5a) are in good general agreement with observations (Figure 4), although some major discrepancies are present (Figure 5b). The three cold spells of the winter 1997/98 (Julian days 355–370, 375–390, 400–415), with low temperatures penetrating deep into the ice, are well simulated. However, the magnitude of the peaks differs from the observations by up to 3°C in the ice and by up to 7°C in the snow. The simulation also captures the persistence of the relatively low temperatures in the ice interior just after surface melt started (Julian days 500–530). This is mainly due to the heat capacity of the ice which increases with increasing temperature and salinity (equation (21)) while the ice thermal conductivity decreases (equation (20)).

[39] The onset of snow melt is captured accurately while the surface ablation is slightly lower than that recorded at gauge 69 (Table 2). Note, however, that the simulated surface melt is sensitive to the value of convergence criteria used for the solution of the internal temperature profile. In all experiments, the total surface melt is independent of the convergence criteria, however the partition of the energy between surface and internal melt can change drastically even for very small temperature changes (see equation (22) for instance). In the situation presented, we obtain a good agreement between simulated and observed surface melts when the brine fraction in the summer does not exceed about 16%. Thus the surface melt presented in this and the following experiments is not considered a validation of the model per se. Instead we use the observations to infer a cap on the maximum allowable brine fraction near the ice surface in the *Bitz and Lipscomb* [1999] brine parameterization scheme.

[40] Simulated temperatures in the upper part of the ice are too low by up to 3°C during the winter months (Julian days 330–390) and around the melt onset (Julian days 510–540) when compared to observations. The difference in winter temperatures at the surface in December and January (Julian days 330–390) is a consequence of the thin snow cover derived from precipitation rates, leading to a deeper penetration of the low surface temperatures down into the ice. In this period, the specified snow cover is significantly lower than that of any individual snow stake at Pittsburgh (e.g., gauge 69). Figure 5b shows that the bottom half of the ice is too warm (by more than 1°C) during most of the simulation period. This difference is due to the fact that the ice thickness measured at gauge 69 is thinner than the "true" ice thickness at the location of the thermistor string (see Figure 4), and that the simulated ice thickness at the thermistor string location is even smaller (see below).

[41] The simulated ice thickness in the control experiment is smaller than that observed throughout the whole year. The

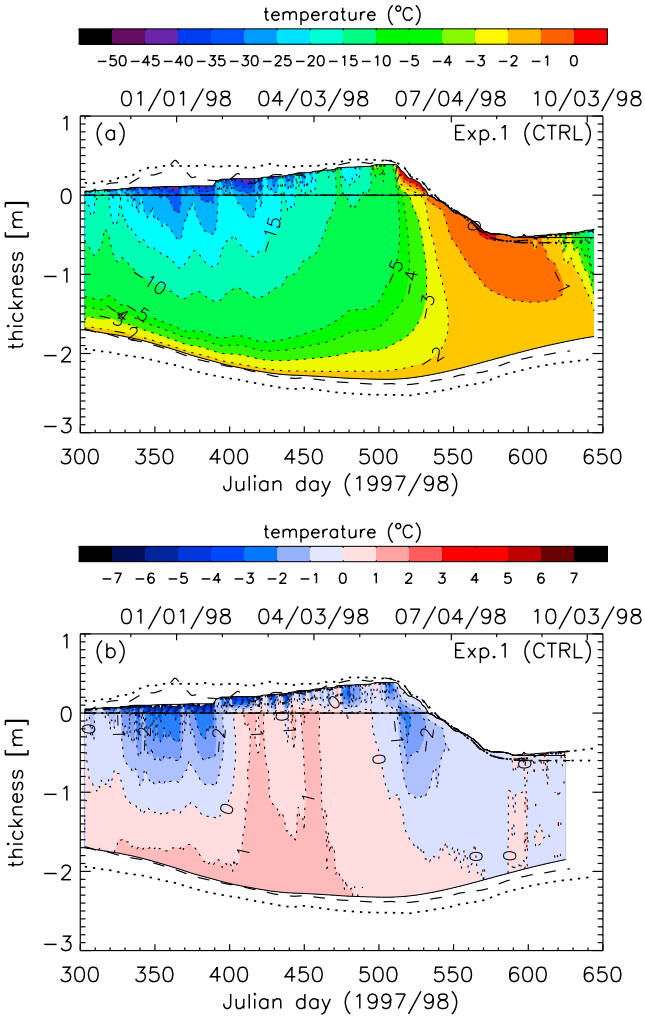

Figure 5. (a) Simulated internal ice temperature and thickness evolution at Pittsburgh for the control experiment. The dashed lines at the surface and base denote the snow and ice thickness measured at gauge 69. The dotted lines indicate the best estimate for the snow surface and ice base as defined by *Huwald et al.* [2005]. (b) Difference between the simulated and observed (Figure 4) internal snow-ice temperature evolution for Pittsburgh.

growth rate is too small during late winter, and the melt rate is too large in summer leading to a gradually increasing discrepancy between the simulated and observed ice thickness. This occurs despite the relatively thin (prescribed) snow cover and low surface ice temperatures in the first 100 days of the simulation which leads to enhanced basal ice growth. Of the main possible errors in physical parameters and forcing fields identified by *Huwald et al.* [2005] (i.e., precipitation, ocean heat flux, and snow conductivity), both the snow conductivity and ocean heat flux could account for the thinner ice cover. However, the fact that the melt rate is too large in the summer (when conductive heat fluxes are small) suggests that the ocean heat flux may be responsible.

[42] Figure 6 presents the evolution of the brine fraction, the ice thermal conductivity, and the amount of energy absorbed in the snow and ice. The brine fraction (Figure 6a) is determined from the internal ice temperature and salinity distribution. It increases with increasing temperature and salinity. As a result, the fraction is close to zero in the upper part of the ice during winter and about 13% near the ice base ($T = -1.6$°C, $S = 4$ psu). During summer, when the internal ice temperature is close to the freezing point, the

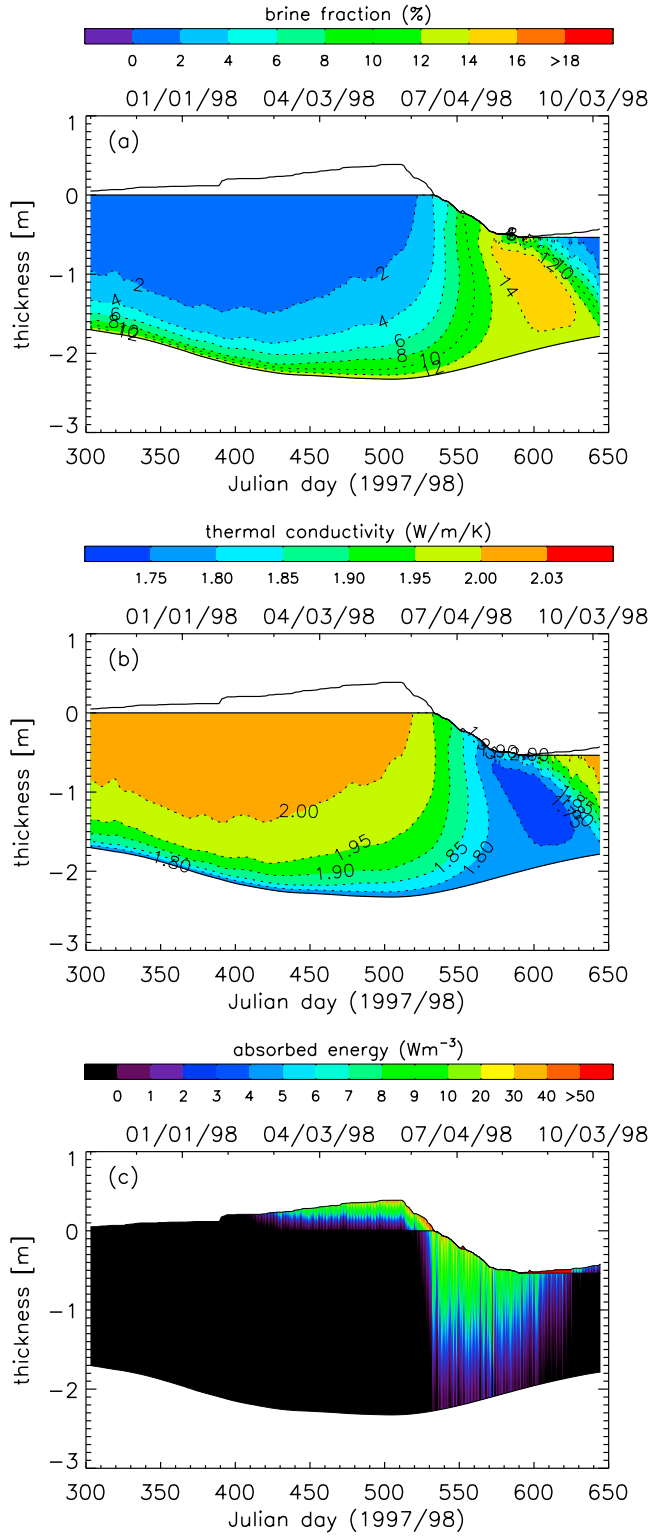

Figure 6. (a) Brine fraction, (b) thermal conductivity, and (c) amount of energy absorbed in the snow and ice (Wm^{-3}).

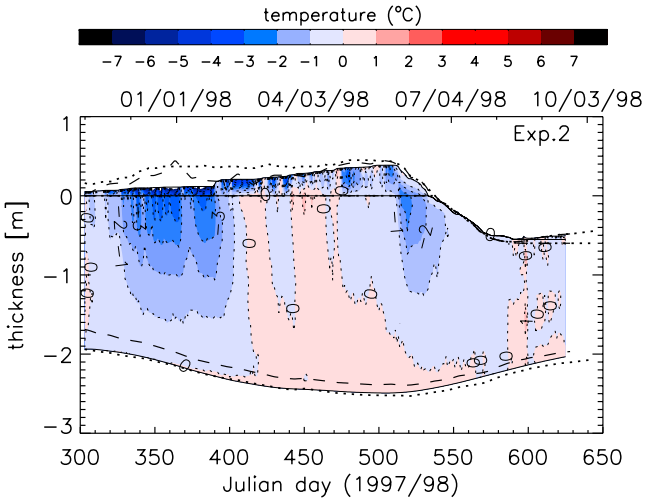

Figure 7. Difference between the simulated and observed internal snow-ice temperature evolution using an initial ice thickness of 194 cm (instead of 170 cm in the control experiment). Dashed lines at the surface and base denote the snow and ice thickness measured at gauge 69. The dotted lines indicate the best estimate for the snow surface and ice base.

fraction reaches a maximum of about 14% over a large part of the ice slab. Figure 6b shows the evolution of the ice thermal conductivity. Both k_i and f_b are strongly dependent on the ice temperature and show a similar pattern.

[43] Figure 6c shows the amount of solar energy locally absorbed in the snow and ice. High-frequency variability associated with the diurnal cycle of shortwave radiation can be seen in this figure. Maximum values are close to 250 Wm^{-3} right at the snow surface and 50 Wm^{-3} at the ice surface. As the applied bulk extinction coefficient for snow (10 m^{-1}) is almost 7 times larger than that of ice (1.5 m^{-1}), transmitted solar radiation is almost completely absorbed in the upper part of the snow cover. Later in the season, when the net shortwave radiation further increases and the snow cover gets thinner, a certain percentage penetrates into the ice. In June and July, when shortwave radiation is at its maximum, a small residual part of the penetrating radiation even reaches beyond the ice base and is absorbed in the ocean. Considering the full period where shortwave radiation is present, the cumulative amount of energy absorbed in the snow, the ice, and the ocean are 21, 60, and 4 MJm^2, respectively. (Note that 10 MJ would heat 1 m^3 of fresh ice by 5.3°C or melt 3.3 cm of fresh ice at 0°C.)

[44] In the next experiment (experiment 2), the best estimate for the initial ice thickness is used (194 cm instead of 170 cm as in the control experiment). Results show internal temperature profiles similar to experiment 1 (see Figure 7), but with a reduced basal ice growth (55 cm as opposed to 63 cm for the control experiment; see also Table 2) due to the thicker initial ice thickness. In all the following experiments, the best estimate of initial ice thickness (194 cm) is used.

4.2. Ocean Heat Flux

[45] The ocean heat flux provided by SIMIP2 (dashed line in Figure 8) is similar to the time series of monthly mean ocean heat fluxes determined at the Pittsburgh site shown by *Perovich and Elder* [2002]. These are computed as a residual of the basal conductive heat flux and the energy of melt. *Huwald et al.* [2005] estimated the ocean heat flux at various heat and mass balance sites at SHEBA in a similar manner. The mean of the ocean heat fluxes derived for five SHEBA sites (Baltimore, Pittsburgh, Quebec 1 and 2 and Seattle) is shown in Figure 8 (thin solid line) together with the ocean heat flux from Pittsburgh (thick solid line) and that provided by SIMIP2. All three curves show the same general pattern with low values at the beginning of the cold season, followed by a peak in March due to storm activity and associated turbulent mixing in the upper ocean. The large summer peak results from solar energy absorbed in open waters mixing down the water column during high wind events and causing under ice melt. The SIMIP2 ocean heat flux reaches its maximum at the beginning of July, a bit earlier than the mean ocean heat flux and the ocean heat flux from Pittsburgh. However, the maxima agree well in amplitude. During spring and summer, both the mean ocean heat flux and the ocean heat flux at Pittsburgh are generally smaller than the ocean heat flux specified by SIMIP2, except for August, where the mean ocean heat flux is larger. The annual mean ocean heat flux at the Pittsburgh site (see Figure 8) is 7.1 Wm^{-2} in contrast to 8.2 Wm^{-2} for that provided by SIMIP2.

[46] Although the two ocean heat fluxes were determined with the same method, differences in the definition of the ice base exact location and assumptions about the temperature and the salinity of newly formed ice (and therefore latent heat of fusion and ice thermal conductivity), can account for the discrepancies. This can be seen more clearly by rewriting equation (4) in terms of the temperature- and salinity-dependent latent heat of fusion and ice thermal conductivity:

$$F_{ocn} = \rho_i L_f(S,T)\,\frac{\partial b_i}{\partial t} + k_i(S,T)\,\frac{\partial T_i}{\partial z}. \qquad (38)$$

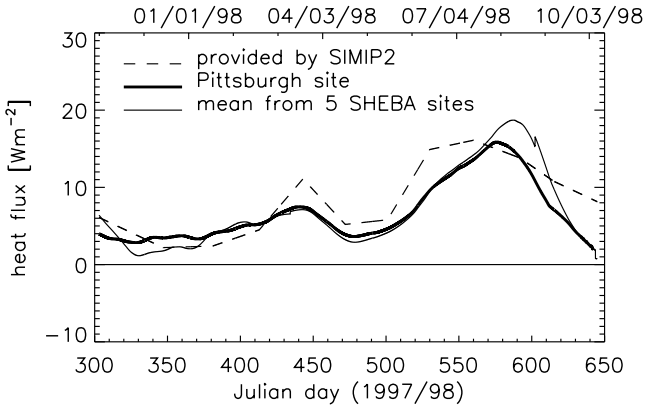

Figure 8. Ocean heat flux (1) provided by SIMIP2, (2) calculated as a residual of the basal conductive heat flux and the energy of melt at the Pittsburgh site, and (3) the mean of ocean heat fluxes calculated at five Surface Heat Budget of the Arctic Ocean (SHEBA) heat/mass balance sites. For both Pittsburgh and the mean ocean heat flux, a salinity of newly formed ice of 10 psu was used.

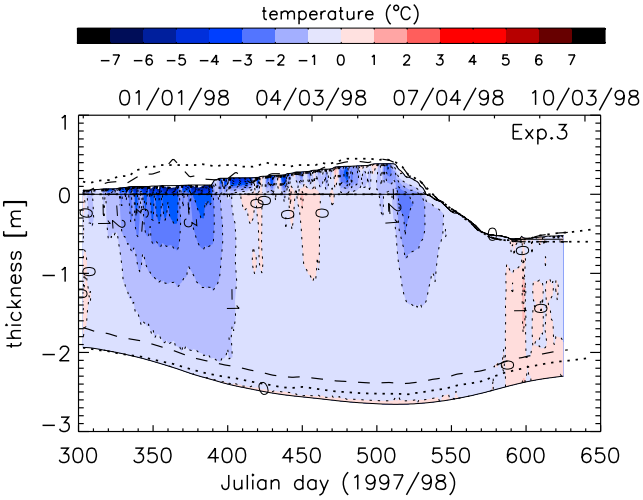

Figure 9. Difference between the simulated and observed internal snow-ice temperature evolution using the ocean heat flux from Pittsburgh (bold line in Figure 8). Dashed lines at the surface and base denote the snow and ice thickness measured at gauge 69. The dotted lines indicate the best estimate for the snow surface and ice base.

The simulated results however are not sensitive to the specified ocean heat flux as long as the salinity of newly formed ice used in the model is consistent with that used to derive the ocean heat flux using the residual method.

[47] Figure 9 presents the simulation results for experiment 3 which uses the ocean heat flux from the Pittsburgh site and a salinity of newly formed ice equal to 10 psu (in accord with the calculation of F_{ocn}). Compared to experiment 2, a significantly thicker ice cover (maximum and final ice thickness) is simulated due to a larger growth rate in winter and a reduced melt rate in summer. The internal temperatures in the snow and ice are similar to those of experiment 1 except in the middle of winter (Julian days 400–520) when the ice is colder due to the increase in ice thickness. In the next section, the effect of the snow cover is investigated. In all the following experiments, the ocean heat flux from the Pittsburgh site is used.

4.3. Snow Cover Evolution

[48] High variability in snow cover thickness at small spatial scales was observed at SHEBA. This together with the fact that the snow depth was not measured at the exact location of the thermistor string leads to major uncertainties in defining the proper snow depth at the thermistor string location. Various methods used to infer the snow depth at the location of the Pittsburgh thermistor string, give considerably different results [*Huwald et al.*, 2005]. Snow depth derived from precipitation rates using constant density is not always realistic as changes in local snow thickness can also occur due to blowing snow, compaction and surface sublimation [*Déry and Tremblay*, 2004]. In contrast with the control experiment which shows a monotonic increase of the snow cover (associated with each snow fall event), measurements show that snow depth at SHEBA sometimes increased or decreased during winter at times when no precipitation was observed.

[49] To evaluate the effect of the snow cover on the thermodynamic evolution of the sea ice, three scenarios using measured or inferred snow covers from the Pittsburgh site are presented. In all three experiments, the mean winter snow cover is thicker than that of the control experiment. Experiment 4a uses the snow thickness measurements from gauge 69, experiment 4b uses the mean snow thickness from gauges 53, 69, and 71 and experiment 4c uses the best estimate of the snow surface evolution, derived from an analysis of the internal snow temperature profiles [*Huwald et al.*, 2005]. Difference plots of internal snow/ice temperatures for the three simulations are shown in Figure 10.

[50] In general, a thicker snow cover leads to higher temperatures in the interior of the snow and ice and consequently to a smaller ice thickness. For instance, a peak in the snow cover at gauge 69 at day 365 leads to higher internal ice temperatures despite the cold air temperature present during that time (Figure 10a). The mean snow thickness from the three gauges in (Figure 10b, experiment 4b) is the thinnest snow cover of all three experiments resulting in the lowest internal ice temperatures, thickest ice, and a realistic representation of both the internal ice temperature and the temporal evolution of the ice base. However, the snow surface temperature is much lower than observed during winter.

[51] The best snow thickness estimate (Figure 10c) results in too high internal ice temperature (1°C at the ice base and 5°C near the ice surface). Consequently the basal growth rate of the ice is substantially reduced. These effects will be compensated by increased snow conductivity as discussed in section 4.4. It is interesting to note that a deep snow cover in spring (e.g., experiment 4a) has only little impact on the basal growth rate since the temperature gradient from the ice base to the surface is smaller during that season. Owing to its higher albedo relative to bare ice, the presence of snow in the spring however has an impact on the timing of the onset of ice surface melt (compare Figure 10b with Figures 10a–10c, for instance).

4.4. Thermal Conductivity of Snow

[52] As discussed in section 3, a snow thermal conductivity of 0.50 $Wm^{-1}\,K^{-1}$ is required to satisfy the continuity of the conductive heat flux at the snow-ice interface at Pittsburgh. This effective conductivity is in contrast to the value of 0.31 $Wm^{-1}\,K^{-1}$ proposed in SIMIP2. The transport of latent heat associated with water vapor diffusion and advective heat transport associated with wind pumping, result in an "effective" thermal conductivity larger than the pure value derived from standard density-conductivity parameterizations [*Sturm et al.*, 1997]. In experiment 5, the higher thermal conductivity of 0.50 $Wm^{-1}\,K^{-1}$ is tested in the model configuration of experiment 4c (Figure 11).

[53] The higher snow thermal conductivity in experiment 5 leads to an enhanced conductive heat transfer in the ice and snow during winter, lower internal ice temperatures and an increased basal growth rate. The simulated internal ice temperature distribution in experiment 5 matches well with the ice temperatures measured at the Pittsburgh site, with differences within ±1°C, except during the period when the snow cover melts (colder by up to 3°C, Figure 11b). The simulated ice thickness also agrees very well with observations with a maximum difference of 4 cm (Table 2).

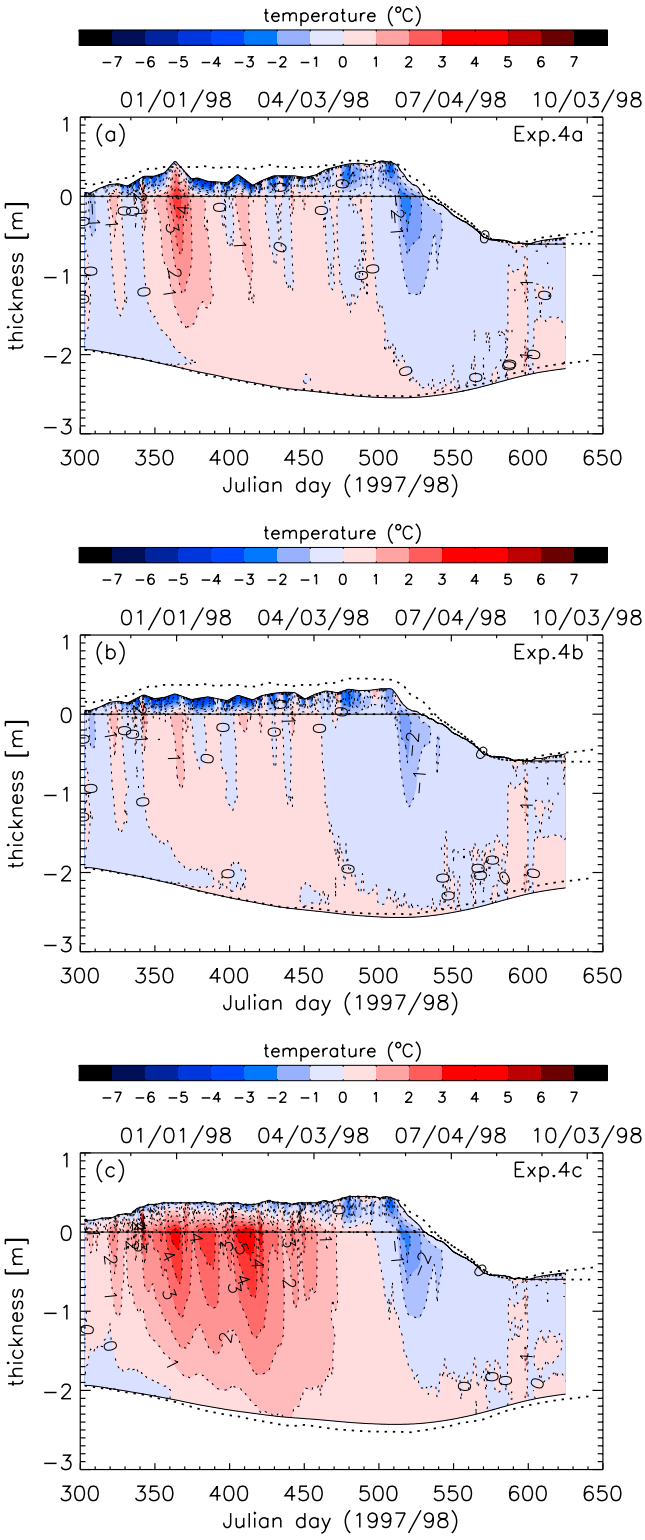

Figure 10. Difference between the simulated and observed snow-ice internal temperature evolution at the Pittsburgh site using the snow thickness specified from (a) thickness gauge 69, (b) the mean of thickness gauges 53, 69, 71, and (c) the best estimate of the snow cover derived from an analysis of internal temperature gradient [*Huwald et al.*, 2005]. Dotted lines indicate best estimates of the observed snow and ice thickness.

Compared to the observed temperature profiles, the snow surface temperature however is generally a bit too low, with differences of up to 3°C. This may be due to the fact that the thermistors have no radiation shielding, and the polyvinyl-chloride rod itself and the wires connecting the thermistors conduct heat. The overall agreement with observations lend support to the corrected forcing field proposed by *Huwald et al.* [2005] and also clearly shows the convenience of using internal snow/ice temperatures to better constrain the validation of thermodynamic sea ice models.

[54] In experiment 6, the model is run adopting the parameters of experiment 5 but with three layers in the ice and only one snow layer. This experiment is conducted to test the model with drastically reduced resolution as is often used in global climate model (GCM) simulations. Results of experiment 6 are very similar to these of experiment 5 (compare Table 2) indicating that the model is not very sensitive to the number of layers used in the

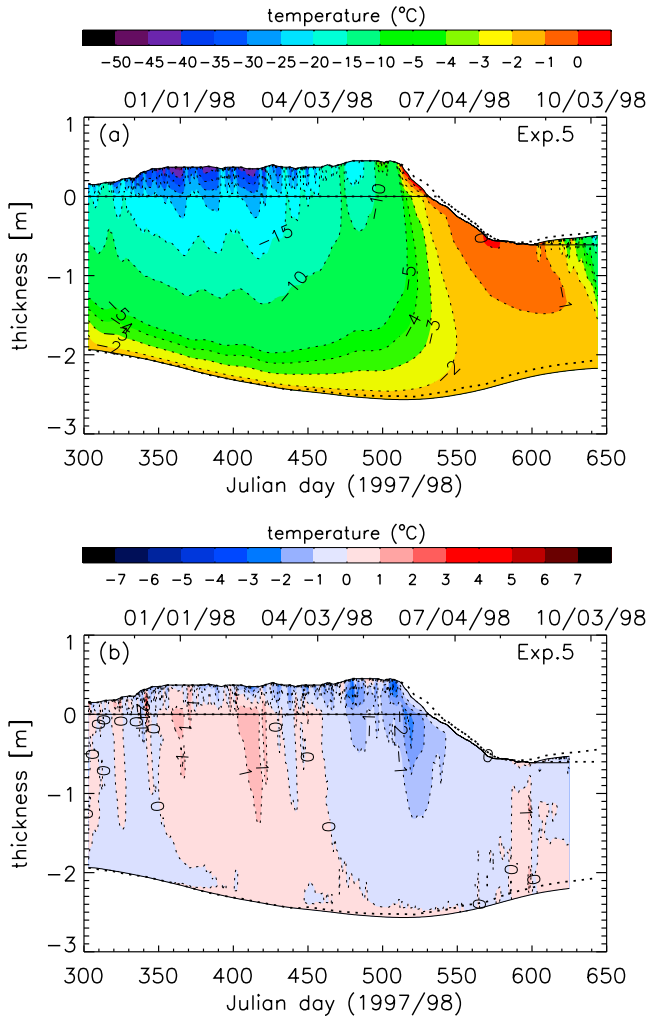

Figure 11. (a) Simulated internal temperature and thickness evolution at the Pittsburgh site using a snow thermal conductivity of 0.50 Wm^{-1} K^{-1} (other forcing and initial conditions as in experiment 4c). (b) Difference between the simulated and observed internal snow-ice temperature evolution. Dotted lines indicate best estimates of the observed snow and ice thickness.

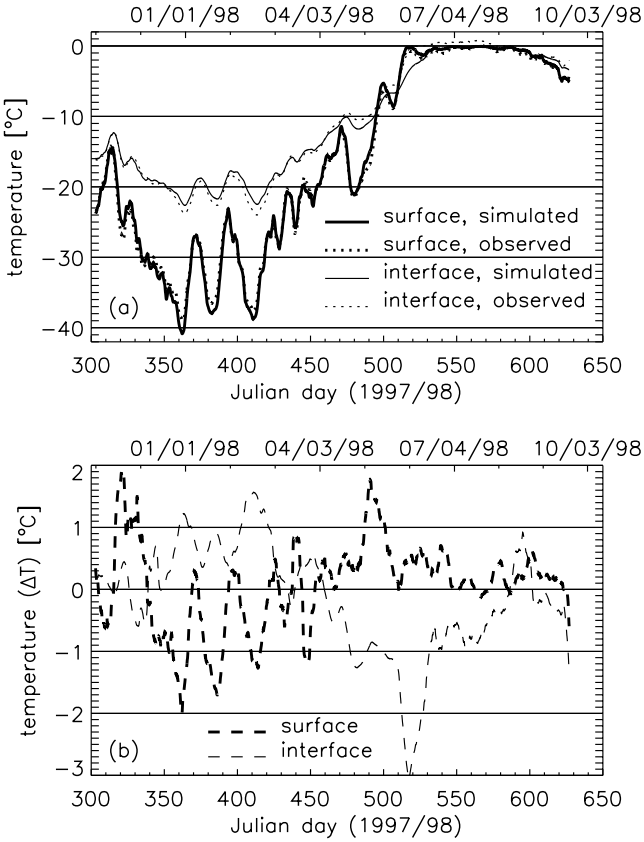

Figure 12. (a) Temporal evolution of (1) the simulated and radiometer-derived skin temperature and (2) the simulated and observed snow-ice interface temperature. (b) Temperature difference between (1) the simulated and observed skin temperature and (2) the simulated and observed snow-ice interface temperature. Time series are smoothed using a 7 day running mean.

simulation. This is due to the fact that a second-order approximation of the temperature gradients at the top and base of the snow and ice leads to calculated conductive heat fluxes of sufficient accuracy. In this model, the way physical processes are described (e.g., brine parameterizations) is more important than the vertical resolution in the snow and ice slabs.

4.5. Consistency Test

[55] In this section, the surface temperature simulated in experiment 5 is compared with the observed skin temperature. Also, a surface energy budget, including longwave and shortwave radiation, the turbulent heat fluxes, the surface conductive heat flux, and the energy of melt, is compared with a similar heat budget calculated at the Pittsburgh location using SHEBA data [*Huwald et al.*, 2005].

[56] In general, the simulated surface temperature (Figure 12) agrees well with the measurements except during three cold periods for short time, when maximum hourly differences of about 2°C are present. During winter, the simulated snow-ice interface temperatures, on the other hand, are generally 0.5°–1.0°C higher than those measured (Figure 12). This suggests that the ratio of the snow and ice thermal conductivities (k_s/k_i) may be even higher than the value reported by *Huwald et al.* [2005] (k_s = 0.50 Wm^{-1} K^{-1}, k_i = 2.034 Wm^{-1} K^{-1}). For instance, a 10% increase of the snow thermal conductivity (i.e., k_s = 0.55 Wm^{-1} K^{-1}) does not significantly change the simulated surface temperature but results in a decrease in snow-ice interface temperature of about 0.5°C, in better general agreement with observations. This results in a larger heat flux through the snow, and an increase in maximum winter ice thickness of 2 cm. Note that the ratio k_s/k_i for the Pittsburgh site reported by *Huwald et al.* [2005] ranges from 0.50 to 0.68 Wm^{-1} K^{-1} depending on the spatial step (Δz) and the order of the differencing scheme used to calculate the temperature gradients in the snow and ice.

[57] The higher temperatures at the snow-ice interface and the (sometimes) lower temperatures at the surface result in a larger temperature gradient across the snow and thus a larger surface conductive heat flux when compared to observations (Figure 13c). The lower simulated surface temperatures during winter also cause a larger simulated downward sensible heat flux (Figures 13d–13f) and a larger net longwave heat flux (Figures 13a–13c) during that time.

[58] Apart from the conductive properties of the snow cover, the surface temperature is naturally determined by the snow and ice thickness. A thin snow cover favors higher surface temperatures, however it results in a deeper penetration of low temperatures during winter leading to a larger temperature gradient in the ice and thus a larger ice thickness. For instance, a simulation with a snow depth half that of the best estimate (not shown here) results in surface temperatures of about 0.5°C warmer during the cold periods in winter, snow-ice interface temperatures about 4°C colder, and an ice thickness 14 cm larger when compared to experiment 5.

5. Conclusions

[59] A new multilayer sigma-coordinate thermodynamic sea ice model is used to simulate the thermodynamic evolution of a snow-covered multiyear ice floe (from October 1997 to October 1998). The model includes penetrating shortwave radiation, a brine pocket parameterization and a coordinate transformation which allows for automatic relayering associated with changes in ice and snow thickness in an energy-conserving manner. This is achieved through an advection term which naturally appears in the transformed energy equation. The model includes all relevant one-dimensional physics of previous thermodynamic models while introducing a more natural framework and easy handling of numerics when compared to previous models. The model is then tested against observations in the context of the Sea Ice Model Intercomparison Project, Part 2, Thermodynamics (SIMIP2) using atmospheric forcing and initial conditions from SHEBA (experiment 1, control experiment). Finally, a series of additional simulations is performed to test the consistency of a corrected data set presented in a companion paper by *Huwald et al.* [2005]. These simulations include sensitivity experiments to the ice thickness (experiment 2), ocean heat flux (experiment 3), snow thickness (experiment 4), and snow thermal conductivity (experiment 5). These experiments are presented to assess both the accuracy of the model simulations and the self-consistency of the SHEBA observations.

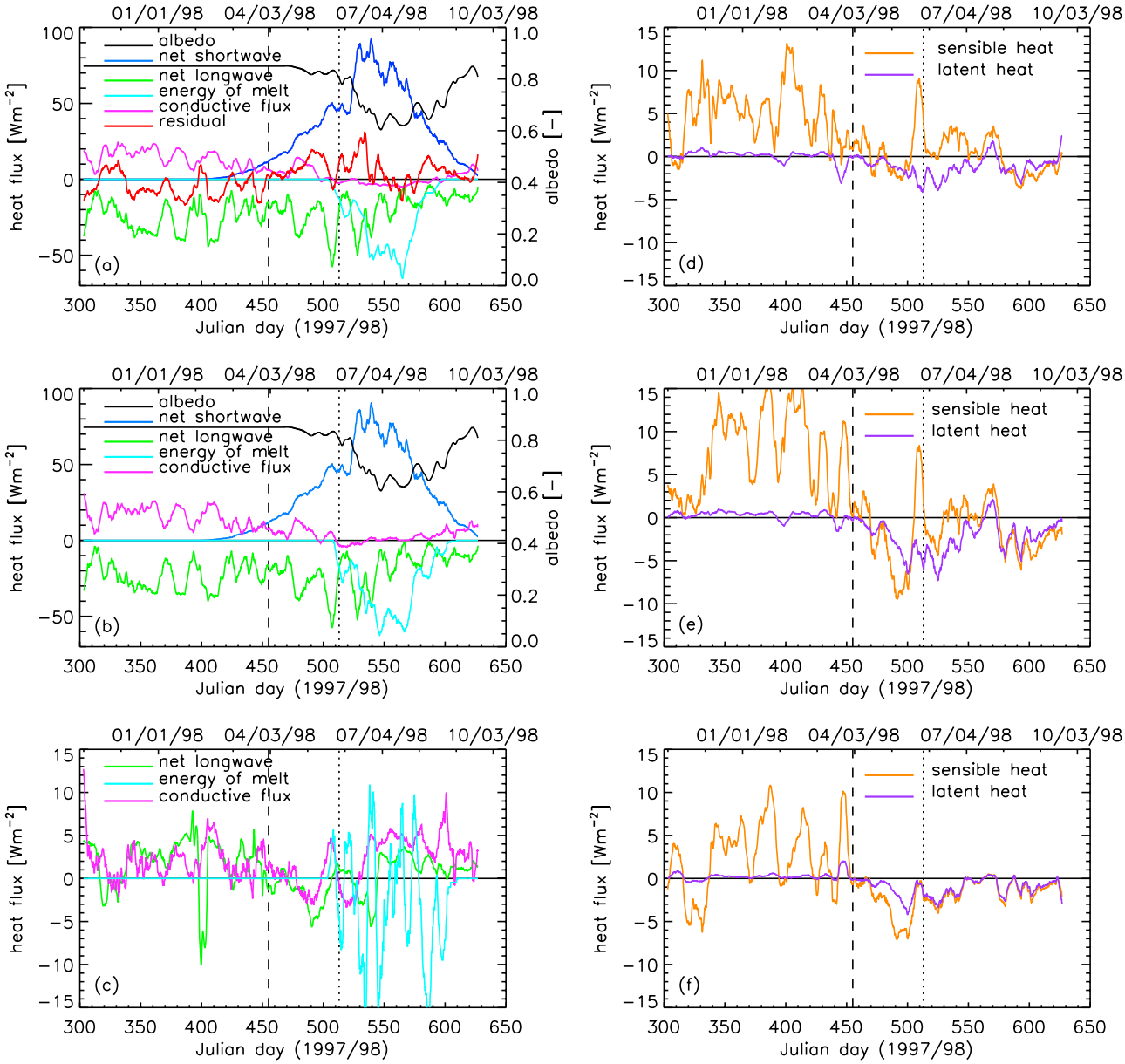

Figure 13. (a, d) Observed and (b, e) simulated surface energy budget (SEB) at the Pittsburgh site (SHEBA). (c, f) Differences between simulated and observed fluxes. Turbulent heat fluxes are shown in separate panels due to their relatively smaller magnitude. The sum of all fluxes is equal to zero in the simulated SEB as it is used explicitly as a surface boundary condition. The dashed line indicates the end of winter and the beginning of summer (here defined as 1 April), and the dotted line marks the onset of surface melt (29 May). Fluxes are smoothed using a 7 day running mean.

[60] Results of the control experiment defined in SIMIP2 show a good general agreement between the simulated and the observed internal snow/ice temperature evolution. However, the simulated internal temperatures are too low by up to 3°C in the upper part of the ice, by up to 7°C in the snow during early winter, and too high by more than 1°C in the bottom half of the ice. The simulated ice thickness remains too small throughout the whole year with too little growth in winter and too large melting in summer.

[61] Simulation results from experiment 2 show that the ice thickness evolution is moderately sensitive to changes in the initial ice thickness (for multiyear ice only). Changes in initial thickness from 170 cm to 194 cm lead to a reduced ice formation during winter by 8 cm and reduced basal summer melt of 1 cm. The results however are very sensitive to the ocean heat flux. Using the corrected ocean heat flux (experiment 3) yields an increase in ice formation by 17 cm during winter, and a decrease in ice melt by 15 cm in summer when compared to experiment 2.

[62] In experiments 4a–4c, three snow cover thickness evolutions were specified: (1) from measurements of an individual thickness gauge (gauge 69), (2) from the mean of three thickness gauges (all located within 1 m of the internal temperature measurements), and (3) a snow thickness evo-

lution derived from an analysis of the internal snow/ice temperature profiles (considered as best estimate). The simulated internal ice temperature and the evolution of the ice base are in good agreement with observations in experiments 4a and 4b, however the simulated snow surface is colder than observed. Prescribing the best estimate snow cover (experiment 4c) yields a maximum ice thickness that is 14 cm smaller compared to that in experiment 4b and internal ice temperatures up to 5°C higher than observed. In general, the thickness of the snow cover has a strong impact on the penetration of the surface temperature signals deep into the ice. This in turn influences the internal snow/ice temperatures which affects the temperature gradient at the ice base and thus basal growth rates. It also has an effect on the timing of the ice melt.

[63] The simulation using a snow thermal conductivity of 0.50 Wm^{-1} K^{-1} (together with the best estimate snow cover, ocean heat flux, and initial ice thickness) results in a very good representation of the internal snow/ice temperature and thickness evolution. The snow and ice thermal conductivities have a large effect on the internal temperature profile and therefore on the basal growth rate during winter. In summer, the melt rates are controlled by the ocean heat flux at the ice base and shortwave radiation at the ice surface. Considering all corrections proposed by *Huwald et al.* [2005], the internal snow/ice temperature evolution is in good agreement with observations (±1°C). The ice thickness evolution is also captured accurately with a maximum difference of 4 cm in winter and 6 cm in summer, when compared with observations. Finally, the onset of ice surface melt and the ice surface ablation agree well with measurements.

[64] The annual mean of the conductive heat flux at the surface (9.3 Wm^{-2}) obtained with a snow thermal conductivity of 0.50 Wm^{-1} K^{-1} is 1.4 Wm^{-2} larger than the corresponding heat conduction with a snow thermal conductivity of 0.31 Wm^{-1} K^{-1}. This difference in the surface conductive heat flux results in a 10 cm (4%) difference in maximum ice thickness (the magnitude of this change depends on the initial snow and ice thickness). The fact that current general circulation models correctly simulate the ice thickness in the Arctic using a somewhat smaller snow thermal conductivity suggests that some other processes may (wrongly) compensate for this difference.

[65] The present study combines both simulation results and a careful heat and mass balance analysis of the SHEBA data to assess the errors in the model and/or inconsistencies in the SHEBA data. In particular it was found that the SHEBA data do not entirely satisfy the prerequisites to perform a high-precision model validation given the high variability at small spatial scales in snow depth and ice thickness. Ideally, snow and ice thickness should be measured at the exact location of the thermistor string. Also, a higher resolution in snow temperature measurements would be useful for a precise evaluation of the conductive heat flux at the snow surface, and the evolution of the snow thermal conductivity. Finally, skin temperature measurements should be made at the location of the thermistor string and more frequent observations of vertical salinity profiles would serve nicely to validate brine parameterization schemes.

[66] **Acknowledgments.** The authors thank the SHEBA principal investigators of the Atmospheric Surface Flux Group (E. L. Andreas, C. W. Fairall, P. S. Guest, P. O. G. Persson), the Ice Physics Group (D. K. Perovich, B. C. Elder, J. Holmgren, J. A. Richter-Menge, M. Sturm, W. B. Tucker), and M. G. McPhee for providing the observational data. In addition, we thank G. M. Flato for providing the SIMIP2 forcing data and G. A. Schmidt for beneficial discussion. We also thank three anonymous reviewers for their helpful suggestions to improve the manuscript. During this work, H. Huwald was supported by the Swiss National Science Foundation, grant 21-59243.99. L.-B. Tremblay was supported by National Science Foundation grants OPP 98-18711 and OPP 02-30264. This is Lamont-Doherty Earth Observatory contribution 6699.

References

Bitz, C. M., and W. H. Lipscomb (1999), An energy-conserving thermodynamic model of sea ice, *J. Geophys. Res.*, *104*, 15,669–15,677.

Bitz, C. M., D. S. Battisti, and R. E. Moritz (1996), Low-frequency variability in the arctic atmosphere, sea ice, and upper-ocean climate system, *J. Clim.*, *9*, 394–408.

Björk, G. (1992), On the response of the equilibrium thickness distribution of sea ice to ice export, mechanical deformation, and thermal forcing with application to the Arctic Ocean, *J. Geophys. Res.*, *97*, 11,287–11,298.

Budyko, M. I. (1972), Future climate, *Eos Trans. AGU*, *35*(10), 868.

Cox, G. F. N., and W. F. Weeks (1988), Numerical simulations of the profile properties of undeformed first-year sea ice during the growth season, *J. Geophys. Res.*, *93*, 12,449–12,460.

Déry, S. J., and L.-B. Tremblay (2004), Modeling the effect of wind redistribution on the snow mass budget of polar sea ice, *J. Phys. Oceanogr.*, *34*, 258–271.

Donn, W. L., and D. M. Shaw (1966), The heat budgets of an ice-free and ice-covered Arctic Ocean, *J. Geophys. Res.*, *71*, 1087–1093.

Ebert, E. E., and J. A. Curry (1993), An intermediate one-dimensional thermodynamic sea ice model for investigating ice-atmosphere interactions, *J. Geophys. Res.*, *98*, 10,085–10,109.

Fichefet, T., and M. A. M. Maqueda (1997), Sensitivity of a global sea ice model to the treatment of ice thermodynamics and dynamics, *J. Geophys. Res.*, *102*, 12,609–12,646.

Fichefet, T., and M. A. M. Maqueda (1999), Modelling the influence of snow accumulation and snow-ice formation on the seasonal cycle of the Antarctic sea-ice cover, *Clim. Dyn.*, *15*, 251–268.

Flato, G. M., and R. D. Brown (1996), Variability and climate sensitivity of landfast Arctic sea ice, *J. Geophys. Res.*, *101*, 25,767–25,777.

Gabison, R. (1987), A thermodynamic model of the formation, growth, and decay of first-year sea ice, *J. Glaciol.*, *33*, 105–119.

Hanesiak, J. M., D. G. Barber, and G. M. Flato (1999), Role of diurnal processes in the seasonal evolution of sea ice and its snow cover, *J. Geophys. Res.*, *104*, 13,593–13,603.

Hindmarsh, R. C. A., and K. Hutter (1988), Numerical fixed domain mapping solution of free-surface flow coupled with an evolving interior field, *Int. J. Numer. Anal. Meteorol.*, *12*, 437–459.

Huwald, H., L.-B. Tremblay, and H. Blatter (2005), Reconciling different observational data sets from Surface Heat Budget of the Arctic Ocean (SHEBA) for model validation purposes, *J. Geophys. Res.*, C05009, doi:10.1029/2003JC002221.

Jenssen, D. (1977), A three-dimensional polar ice-sheet model, *J. Glaciol.*, *18*, 373–389.

Launiainen, J., and B. Cheng (1998), Modelling of ice thermodynamics in natural water bodies, *Cold Reg. Sci. Technol.*, *27*, 153–178.

Maykut, G. A., and N. Untersteiner (1971), Some results from a time dependent thermodynamic model of sea ice, *J. Geophys. Res.*, *76*, 1550–1575.

Mellor, G. L., and L. Kantha (1989), An ice-ocean coupled model, *J. Geophys. Res.*, *94*, 10,937–10,954.

Murray, F. W. (1967), On the computation of saturation vapor pressure, *J. Appl. Meteorol.*, *6*, 203–204.

Ono, N. (1967), Specific heat and heat of fusion of sea ice, in *Physics of Snow and Ice*, vol. 1, edited by H. Oura, pp. 599–610, Inst. of Low Temp. Sci., Hokkaido, Japan.

Parkinson, C. L., and W. M. Washington (1979), Large-scale numerical model of sea ice, *J. Geophys. Res.*, *84*, 311–337.

Perovich, D. K., and B. C. Elder (2001), Temporal evolution of Arctic sea-ice temperature, *Ann. Glaciol.*, *33*, 207–211.

Perovich, D. K., and B. C. Elder (2002), Estimates of the ocean heat flux at SHEBA, *Geophys. Res. Lett.*, *29*(9), 1344, doi:10.1029/2001GL014171.

Perovich, D. K., T. C. Grenfell, B. Light, J. A. Richter-Menge, M. Sturm, W. B. Tucker III, H. Eicken, G. A. Maykut, and B. Elder (1999), *SHEBA: Snow and Ice Studies* [CD-ROM], Cold Regions Res. and Eng. Lab., Hanover, N. H.

Persson, P. O. G., C. W. Fairall, E. L. Andreas, P. S. Guest, and D. K. Perovich (2002), Measurements near the Atmospheric Surface Flux

Group tower at SHEBA: Near-surface conditions and surface energy budget, *J. Geophys. Res.*, *107*(C10), 8045, doi:10.1029/2000JC000705.
Phillips, N. A. (1957), A coordinate system having some advantages for numerical forecasting, *J. Meteorol.*, *14*, 184–185.
Schmidt, G. A., C. M. Bitz, U. Mikolajewicz, and L.-B. Tremblay (2004), Ice-ocean boundary conditions for coupled models, *Ocean Modell.*, *7*, 59–74.
Schwerdtfeger, P. (1963), The thermal properties of sea ice, *J. Glaciol.*, *4*, 789–807.
Semtner, A. J. (1976), A model for the thermodynamic growth of sea ice in numerical investigations of climate, *J. Phys. Oceanogr.*, *6*, 379–389.
Sturm, M., J. Holmgren, M. König, and K. Morris (1997), The thermal conductivity of seasonal snow, *J. Glaciol.*, *143*, 26–41.
Sturm, M., J. Holmgren, and D. K. Perovich (2002a), Winter snow cover on the sea ice of the Arctic Ocean at the Surface Heat Budget of the Arctic Ocean (SHEBA): Temporal evolution and spatial variability, *J. Geophys. Res.*, *107*(C10), 8047, doi:10.1029/2000JC000400.
Sturm, M., D. K. Perovich, and J. Holmgren (2002b), Thermal conductivity and heat transfer through the snow on the ice of the Beaufort Sea, *J. Geophys. Res.*, *107*(C10), 8043, doi:10.1029/2000JC000409.
Ukita, J., and D. G. Martinson (2001), An efficient adjustable-layering thermodynamic sea-ice model formulation for high-frequency forcing, *Ann. Glaciol.*, *33*, 253–260.
Untersteiner, N. (1961), On the mass and heat budget of Arctic sea ice, *Arch. Meteorol. Geophys. Bioklimatol., Ser. A*, *12*, 151–182.
Walsh, J. E. (1983), The role of sea ice in climate variability: Theory and evidence, *Atmos. Ocean*, *3*, 229–242.

H. Blatter, Institute for Atmospheric and Climate Science, Swiss Federal Institute of Technology, Winterthurerstrasse 190, CH-8057 Zurich, Switzerland. (blatter@env.ethz.ch)

H. Huwald, Environmental Fluid Mechanics Laboratory, Ecole Polytechnique Federale de Lausanne, Station 2, CH-1015 Lausanne, Switzerland. (hendrik.huwald@epfl.ch)

L.-B. Tremblay, Lamont-Doherty Earth Observatory of Columbia University, Route 9W, Palisades, NY 10964-8000, USA. (tremblay@ldeo.columbia.edu)